International Journal of Coal Geology 211 (2019) 103210

Contents lists available at ScienceDirect

International Journal of Coal Geology

journal homepage: www.elsevier.com/locate/coal

Reassessment of coal permeability evolution using steady-state flow methods: The role of flow regime transition

Linsen Wang[a], Zhongwei Chen[a,b], Chunguang Wang[a,c,*], Derek Elsworth[d], Weitao Liu[a]

[a] State Key Laboratory of Mining Disaster Prevention and Control Co-founded by Shandong Province and the Ministry of Science and Technology, Shandong University of Science and Technology, China
[b] School of Mechanical and Mining Engineering, The University of Queensland, St Lucia, QLD 4074, Australia
[c] State Key Laboratory of Geomechanics and Geotechnical Engineering, Chinese Academy of Sciences, Institute of Rock and Soil Mechanics, Wuhan 430071, China
[d] Energy and Mineral Engineering & Geosciences, G3 Center and EMS Energy Institute, Pennsylvania State University, Pennsylvania, PA 16802-5000, USA

ARTICLE INFO

Keywords:
Slip flow
Apparent permeability
Effective stress
Knudsen number

ABSTRACT

Steady-state flow methods are widely applied in the laboratory where permeability evolution is typically evaluated assuming a uniform pressure gradient along the sample. The accuracy of this approach is questionable for tight geomaterials when gas is used as the injecting fluid, due to: (i) the nonlinear distribution of pore pressure and gradient along the sample, suggesting that (ii) both slip and viscous flow may occur concurrently within samples containing nano-pores. The following presents laboratory permeability measurements integrated with numerical analysis to investigate the evolution of coal permeability under different flow regimes. Measured coal permeability first decreases and then rebounds as gas injection pressure is reduced, indicating the transition in flow regime from viscous to slip dominant. Numerical results chart the nonlinear distribution of pore pressure along the sample and the spatial transition of flow regimes determined by controlling the magnitude of the injection pressure. When injection pressure is below the threshold for slip flow, then slip flow dominates throughout the entire coal sample and apparent permeability increases significantly along the gas flow direction. The relative contribution of the slip flow to total flow increases with the reduction in pore pressure, increasing from 0.02 to 0.18 for the tested sample. Results also show that the conventional method of plotting apparent permeability against the mean experimental pressure always gives a greater permeability than the two alternate methods proposed in this work, and the discrepancy increases with increasing injection pressures (up to 7.66% when pore pressure = 6 MPa). Uncertainty analysis is strongly recommended when measuring permeability of tight rocks using this experimental method.

1. Introduction

Coalbed methane (CBM) is a substantial unconventional gas resource. Coal permeability plays an important role in controlling CBM reservoir productivity. Coalbed reservoirs typically comprise matrix blocks encased within a cleat system with permeability more sensitive to stress than conventional gas reservoirs due to the presence of the stress-sensitive cleats (Pattison et al., 1996; Laubach et al., 1998; Somerton et al., 1975a; Gray, 1987; Shi and Durucan, 2005; Pan and Connell, 2012). During CBM extraction, reservoir depletion and the related drop in reservoir pressure triggers gas-coal interactions involving the compression of pores/cleats and gas desorption/−induced matrix shrinkage(Gasparik et al., 2014; Heller et al., 2014a; Fan et al., 2018). These gas-coal interactions complicate gas transport mechanisms, and in turn present a challenge in the accurate prediction of coal permeability.

Significant effort has focused on the investigation of the relationship between coal permeability and pore pressure. To investigate the *impacts of effective stress and gas sorption* on coal permeability, two alternate stress-controlled conditions are usually applied (Rui et al., 2018). One condition is to keep the confining stress (or pore pressure) constant in order to measure the influence of effective stress on the pore/fracture network within the coal (Wang et al., 2015; Harpalani and Schraufnagel, 1990; Robertson and Christiansen, 2005; Pini et al., 2009; Gensterblum et al., 2014a; Wang et al., 2017; Wang et al., 2011; Han et al., 2010; Cui et al., 2018).

Under constant confining stress with increasing pore pressure (i.e., injecting gas into the sample) coal permeability may either decrease, as

* Corresponding author at: State Key Laboratory of Mining Disaster Prevention and Control Co-founded by Shandong Province and the Ministry of Science and Technology, Shandong University of Science and Technology, China.
E-mail address: cgwang@sdust.edu.cn (C. Wang).

https://doi.org/10.1016/j.coal.2019.103210
Received 4 February 2019; Received in revised form 27 May 2019; Accepted 28 May 2019
Available online 30 May 2019
0166-5162/

the gas sorption effect dominates, or initially decrease and then rebound as the impact of the reduction in effective stress ultimately dominates. For gas depletion, the opposite response is observed. Alternatively, effective stress (conventionally defined as the difference between confining stress and pore pressure) may be retained constant to measure the impact of gas adsorption/desorption–induced matrix swelling/shrinkage, alone, on the coal permeability (Pan et al., 2010; Harpalani and Chen, 1997a; Chen et al., 2011; Li et al., 2013; Anggara et al., 2016; Meng and Li, 2017; Feng et al., 2017; Seomoon et al., 2015). Under this condition (constant effective-stress), coal permeability normally decreases with an increase in pore pressure and vice versa for desorption. Nevertheless, it is commonly observed that, when pore pressure is below a certain value, coal permeability is inversely correlated with pore pressure. This phenomenon is usually considered as the effect of matrix shrinkage due to gas desorption but overlooks the influence of gas slippage. As the mean free path of gas molecular transport is inversely proportional to gas pressure, at lower pressures, the mean free path increases and may reach and exceed the characteristic length (diameter) of the gas flow conduit. Under this condition, the gas molecules will frequently collide with the walls of the flow channel and trigger the transition from Darcy flow to gas slip flow (Klinkenberg, 1941a; Cui and Bustin, 2005; Fink et al., 2017; Vadpour, 2009; Civan, 2010; Ziarani and Aguilera, 2012; Klinkenberg, 1941b; Wang et al., 2016a). Such effects are commonly observed in helium permeability experiments investigating slip flow or the Klinkenberg effect (Pini et al., 2009; Gasparik et al., 2013; Heller et al., 2014b; Zhang et al., 2015).

Laboratory investigations exploring such transitions in flow behavior – both mechanical and flow-regime-related – are usually conducted under either transient flow (Brace et al., 1968a; Bourbie and Walls, 1982; Kumar et al., 2016; Hsieh et al., 1981; Pan and Connell, 2015) or steady-state flow conditions (Jones and Meredith, 1998; Chen, 1994a; Harpalani and Chen, 1997b; Li et al., 2009b; Tanikawa and Shimamoto, 2009; Amann-Hildenbrand et al., 2012). The former is more common in measuring the permeability of tight rocks while the latter is more suitable for highly permeable geo-materials. Despite this, steady state methods are still widely used in tight rocks such as coal and shale, largely due to the simplicity of the measurement system and the resulting data analysis. Steady-state flow is conducted at a prescribed pressure gradient or an equilibrium pore pressure (Brace et al., 1968b), in which case the measured permeability can be treated as an overall property of the sample at the average pressure (i.e., mean value of inlet and outlet pressures). The process is repeated to recover permeability measurements over a range of average pore pressures to define the sensitivity of permeability to both pressures and effective stresses – as necessary for various reservoir engineering purposes, e.g. reservoir simulation and production analysis.

This steady measurement method has two key issues: (i) it assumes that the flow regime is viscous only and overlooks the effect of slip flow that commonly occurs in tight rocks; and (ii) the use of average pore pressure assumes that the pore pressure distribution along the flow direction is linear, which is not the case when the fluid is a compressible gas. This nonlinear distribution of pore pressure may result in a misalignment of the pore pressure with the correspondingly-recovered pressure-dependent permeability magnitudes. The literature that quantifies the magnitude of this misalignment between measured permeability and actual pore pressure by accommodating the transition between flow regimes is scant – since multiple flow regimes are sometimes present within a single sample and experiment and therefore the permeability results are composite and confused.

In this study, we define the uncertainty in permeability -versus- pore pressure characteristics associated with the use of the steady-state flow method related to the presence of multiple flow regimes within a single sample. This is achieved by integrating experimental and numerical approaches. Experiments first define the relationship between overall permeability of a sample and various injection pressures under constant confining pressure. Numerical models are then applied that map the correct flow regime along the sample (including Knudsen slip flow where pressures are sufficiently low) and then correct the apparent permeability where viscous, slip and poromechanical effects may all be manifest. The form of the permeability-pressure curve and the characteristics of the evolution of flow regime transition are explored and their impact on apparent permeability is then discussed.

2. Experiment setup and procedures

2.1. Coal sample characterization

Permeability measurements are completed on high-volatile bituminous coal (2.5 cm in diameter and 5.0 cm in length) cored from a block collected from the Juye coalfield in eastern China.

Porosity structure of coal is significantly related to the coal permeability. In order to assess cleat/pore connectivity for the coal sample, two types of CT scanning were conducted by a NanoVoxel-2000 X-ray machine, Sanying Precision Instruments *Co.*, Ltd. The Type I was to scan the full-sized coal sample with a resolution of 13 μm (using a Flat Panel Detector); the Type II was to scan a 3 mm diameter offcut with a resolution of 0.5 μm (using an Optocoupler Detector). Associated running parameters of the X-ray machine are listed in Table 1.

Fig. 1 shows analysis results of two CT scan datasets. As shown in Fig. 1a, a cylindrical digital-image was reconstructed from the voxel data of the full-sized coal sample, where the white part is minerals. Threshold segmentation was used to define the microstructure of the coal sample from the voxel data. The associated spatial distributions of pores colored by red are given in Fig. 1b. Mean porosity of each cross sectional image along the axial of the sample is plotted in Fig. 1c. The mean porosity of the overall coal sample is 0.07%. It seems to indicate that the coal sample has few visible cleats. Results from Type I scan show that few connected micro-fissures exist in the coal sample, and no cleats were detected.

The results from Type II scan are plotted in Fig. 1d and Fig. 1e, showing pore structure information of the coal offcut (1 mm) with the resolution of 0.5 μm. The mean porosity of the Type I slices is 1.42%, which is 20.3 times of porosity for Type II results, indicating that the contribution by larger pores (> 13.37 μm) to the total flow is highly likely minimal.

In addition, Fig. 1f plots amounts of various-sized pore per volume under the two scanning resolution conditions. It can be clearly seen that the amount of pore with 1-2 μm is the largest group among the coal sample. The coal sample could be reasonably treated as a tightly compacted media, because few visible macro-fissures exist in the microstructure at a voxel resolution of 13 μm. These results indicate that the transport capacity of the coal sample is mainly dependent on pore, and the impact of cleats on gas flow is expected to be minimal.

Pore size is an important parameter as it determines the effect of slip flow on overall flow in narrow channels. The maximal balls method was used to evaluate the pore and pore-throat statistics(Silin and Patzek, 2006). Fig. 2 illustrates the distribution of pores and pore throat radii for the Type II scan, indicating the predominance of both pores and pore throats in the range 1–2 μm. The statistical parameters of the pore throats are listed in Table 2.

Table 1
Running parameters for two types of CT scanning.

Size of sample (mm)	Running parameters of CT machine	Resolution (μm)	Mean porosity (%)
25	Voltage:80 kV Current:80 μA	13.37	0.07
3.0	Voltage:50 kV Current:90 μA	0.50	1.42

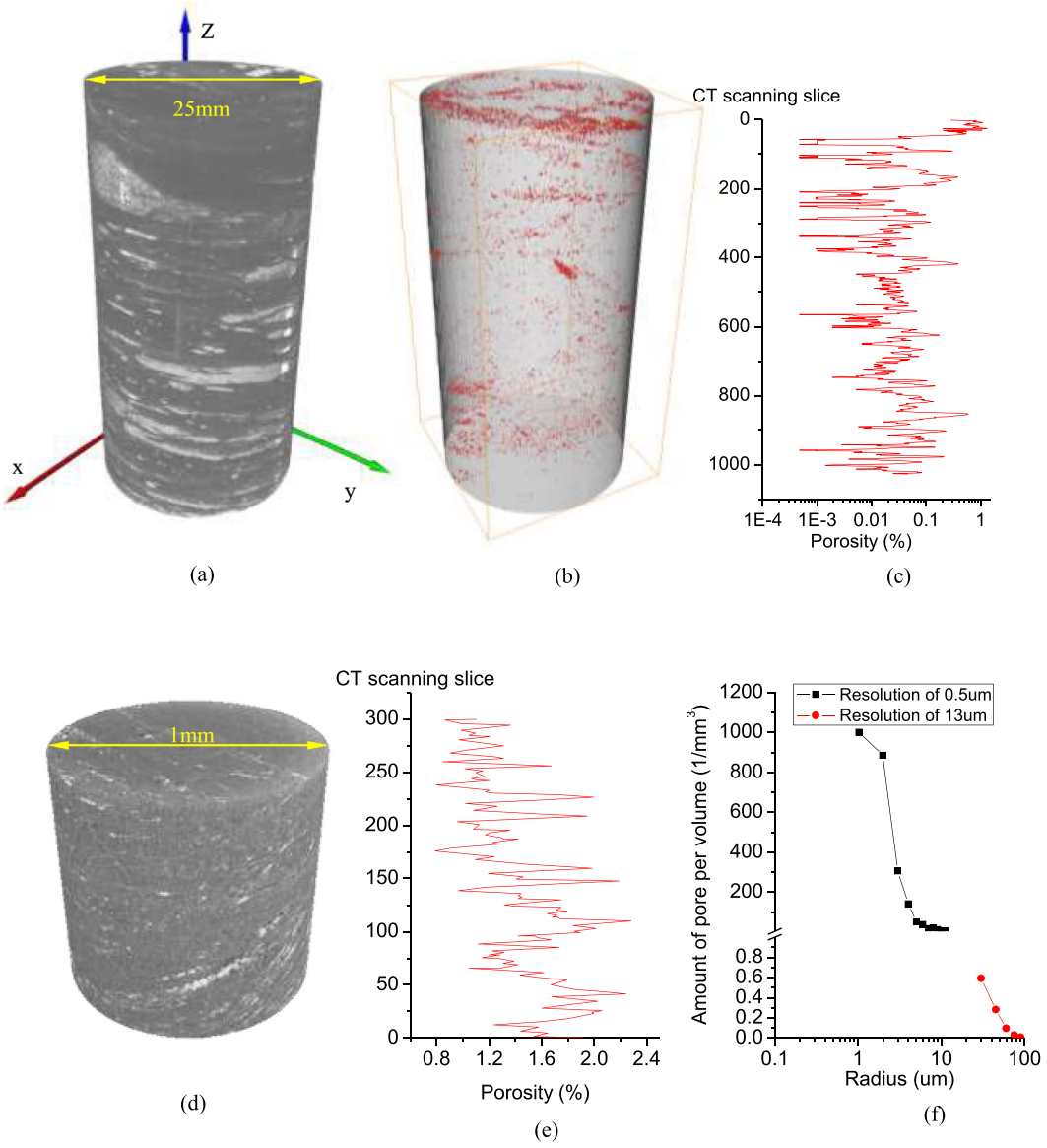

Fig. 1. Type I scan results: (a) a fully-sized CT images; (b) the spatial distribution of pore in 3D; (c) spatial distribution of porosity of the full-sized coal. Type II scan results: (d) a three-dimensioal resconstructed image of the coal offcut (1 mm off 3 mm sample); (e) porosity of cross section image of the offcut coal; and (f) pore amount per volume.

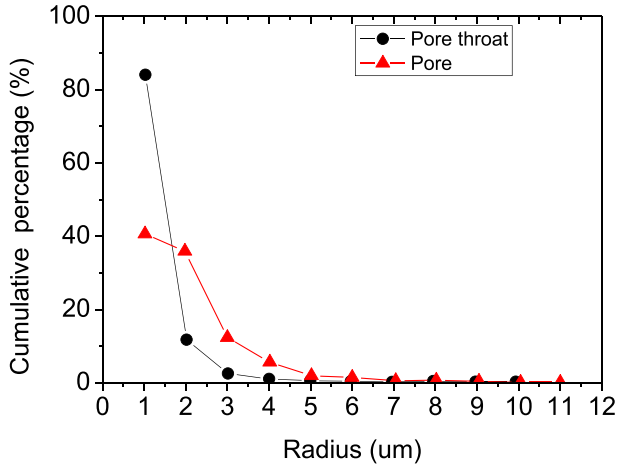

Fig. 2. Size distributions of pore and pore throat of the coal sample.

Table 2
Summary of pore and pore throat statistics recovered from X-ray CT image analysis.

Parameter	Value
Maximum radius of pore throat (μm)	9.87
Mean radius of pore throat (μm)	0.96
Maximum length of pore throat (μm)	19.44
Mean length of pore throat (μm)	3.13
Maximum ratio of pore radius to pore throat radius	23.29
Mean ratio of pore radius to pore throat radius	3.13
Mean volume of pore throat (μm^3)	98.43

2.2. Experimental arrangement

Helium permeability measurements are completed using the steady-state method. The experimental setup (Fig. 3) consists of a Hassler-type core holder, two syringe pumps and the measurement of fluid flow rate. One syringe pump applies the confining pressure to the cylindrical sample and a second applies the injection pressure. The downstream

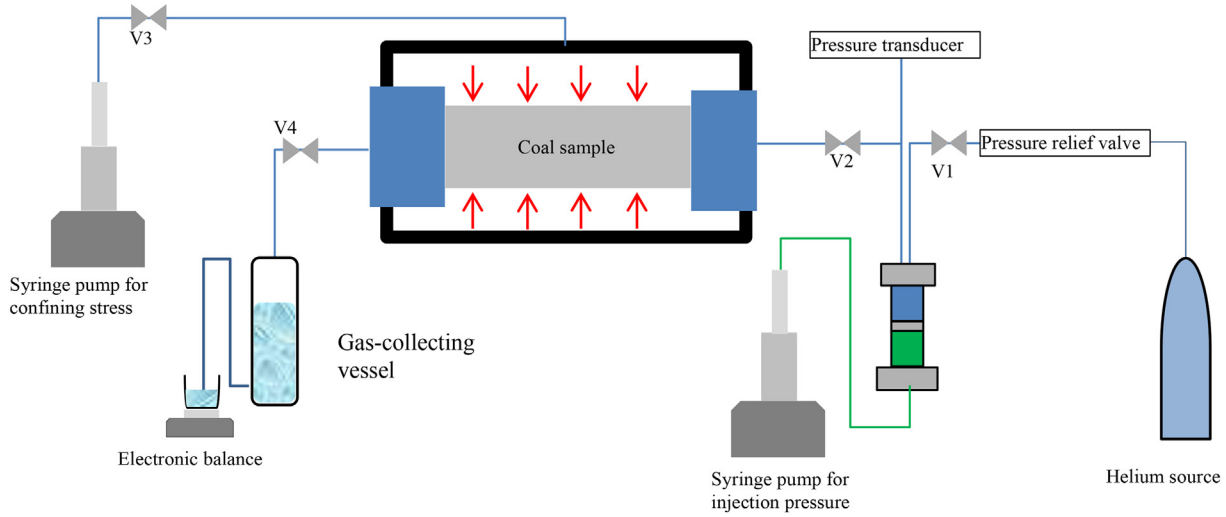

Fig. 3. Schematic diagram of experimental apparatus.

reservoir exits into a fluid measurement unit with gas flow rate determined by water displacement. The expelled water from the sample is collected and weighed by electronic balance (Sartorious BSA223S-CW) with the accuracy of 1.0 mg.

The measurement accuracy of the steady state method depends on flow rate,(Malkovsky et al., 2009) and its accuracy decreases with decreasing flow rate, particularly for very tight rocks or extremely slow flow rates. In order to calibrate this experimental setup, a series of benchmark tests were conducted on three known-permeability standards, as shown in Fig. A1 (Appendix). Three standard samples were used as comparison with the cumulative mass of the drained water during each test shown in Fig. A2. The results are compared in Fig. A3 and summarized in Table A1, showing that the measured permeability data from the experimental setup are consistent with the standard values, confirming the reliability of the apparatus.

In a single experiment, the desired confining pressure is first applied, and the sample saturated with helium. Both the confining pressure and the initial pore pressure are left to equilibrate for at least one week to both minimize the impacts of creep deformation within the sample and to check for leaks. The steady state experiment begins by opening the downstream valve V4 to release the gas stored in the coal sample, during which the upstream gas pressure is retained constant and equal to the pore pressure of the coal sample at equilibrium. The downstream gas pressure of the coal sample is set to atmospheric with gas density defined by the PVT characteristics of helium. When volumetric flow rate becomes constant, coal permeability can be calculated as (Somerton et al., 1975b; Chen, 1994b):

$$k_{app} = -\frac{Q_{out}\cdot\mu\cdot L}{A}\cdot\frac{2P_d}{(P_d^2 - P_u^2)} \quad (1)$$

where Q_{out} (m^3/s) is outflow rate of the effluent gas, A (m^2) is the cross sectional area of the coal sample, L (m) is the overall length of the coal sample, P_d (Pa) is the downstream pressure and P_u (Pa) is the upstream pressure, equal to 1 atm. The outflow rate of helium is the mean steady-state flow defined as the ratio of the volume of helium flow to the flow duration (Eq. (2)):

$$Q_{out} = \frac{\Delta V}{\Delta T} = \frac{V_t - V_0}{t - t_0} \quad (2)$$

The decremented gas pressure injection sequence (from 6 MPa to 0.5 MPa) under a predetermined constant confining pressure (8 MPa and 12 MPa) is illustrated in Fig. 4.

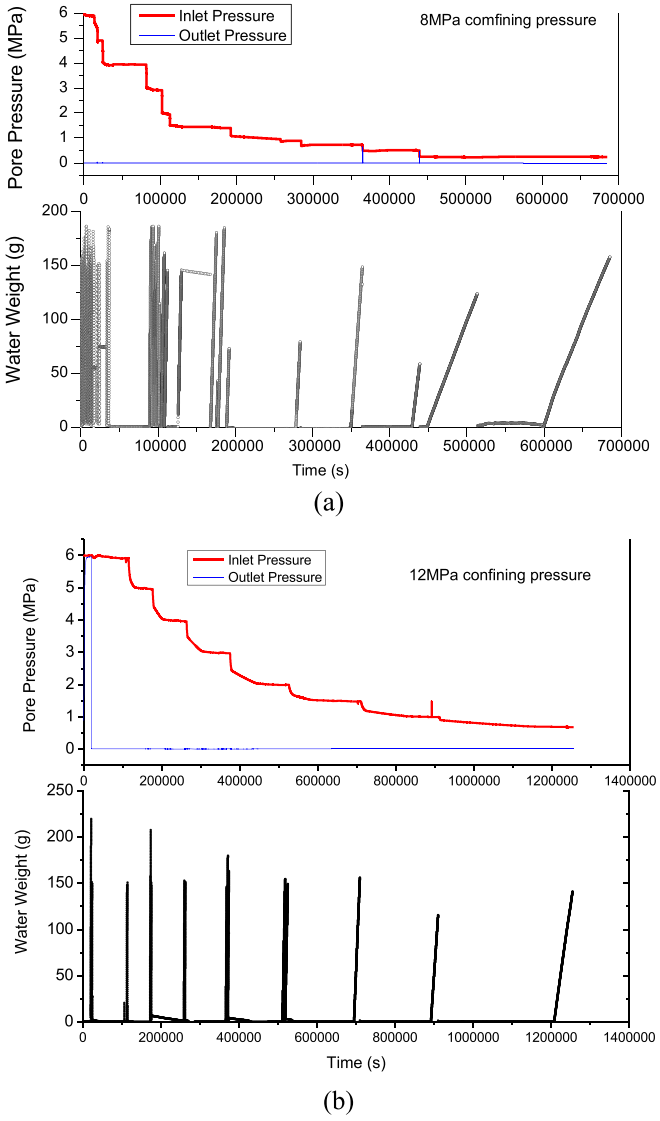

Fig. 4. Loading sequence of injection pressures under different confining pressures. (a) for injection pressure path under the 8 MPa confining pressure; (b) for injection pressure path under the 12 MPa confining pressure.

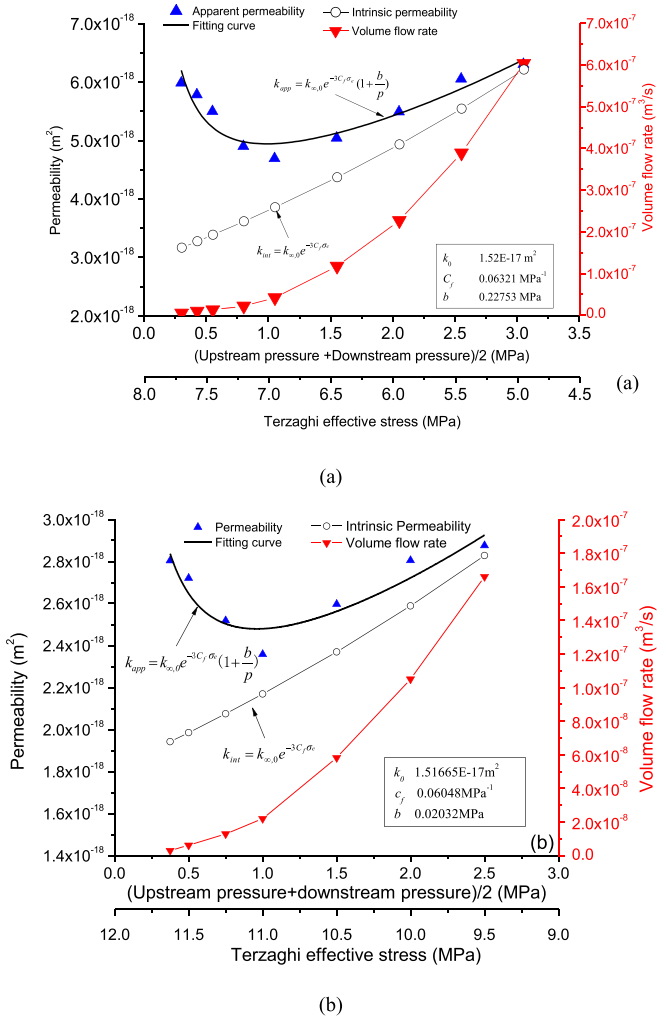

Fig. 5. Measured permeability and calculated intrinsic permeability vs. mean pore pressure and Terzaghi effective stress for confining stresses of (a) 8 MPa, and (b) for 12 MPa.

2.3. Experimental results

The evolution of both helium gas outflow rates and the measured permeability with mean pore pressure are plotted in Fig. 5a and Fig. 5b, respectively. At any fixed confining stress, the measured permeability values for both confining stresses first decrease and then rebound as the mean pore pressure drops. The rebound in permeability as pressures decreases and effective stress increases cannot be explained by the impacts of coal swelling in a deformable medium as the permeating gas in non-sorbing (and therefore non-swelling). One potential reason for this abnormal behavior is the transition in flow regime which dominates relative to poromechanical effects. Increasing effective stress reduces the size of the micropores in coal matrix, which consequently makes the size of the pores comparable to the mean free path of the gas. This occurs at the same time that the pressure is reduced and slip flow also becomes a more important mode of transport. Thus, both effects are additive and together potentially drive the transition to slip flow. Under these conditions, the collisions of gas molecules with the pore walls must be taken into account. The gas slippage phenomenon was first documented by Klinkenberg, as described by Eq. (3), which directly couples the poromechanical pore structural changes and effective stress together with the impacts of slip flow (Gensterblum et al., 2014b):

$$k_{app} = k_{\infty,0} e^{-3C_f \sigma_e}\left(1 + \frac{b}{p}\right) \quad (3)$$

where k_{app} (m^2) is apparent permeability, $k_{\infty,0}$ (m^2) is the Klinkenberg-corrected permeability (or intrinsic permeability) at zero effective stress, b (MPa) is the gas slippage factor and c_f (MPa^{-1}) is a stress coefficient. The experimental results are shown in Fig. 5 and fitted to Eq. (3). A stress-dependent intrinsic permeability (assuming Terzaghi's principle of effective stress) is also predicted by the fitting parameters involving $k_{\infty,0}$ and c_f. It is apparent from Fig. 5 is that the intrinsic permeability (k_{int}) decreases with increasing effective stress, which can be directly validated by the reduction in the measured gas flow rate. The relation between the measured permeability and effective stress is a macroscopic reflection of gas molecular motion and pore wall effects at a given stress condition.

Nevertheless, this relation is unable to characterize a spatio-temporal evolution of coal permeability, particularly the evolution of coal permeability prior to equilibrium. Therefore, the following adopts a numerical approach to analyze the dynamic gas flow behavior across the entire coal sample in an effort to gain insights into fluid transient flow behavior.

3. Numerical model implementation and validation

The data acquired from the measurements using steady-state flow methods are only able to evaluate representative permeability of the sample for an assumed mean pore pressure at the equilibrium state. Nevertheless, during gas depletion, the pore pressure continues to change, resulting in changes in the effective stress and in coal microstructure. As a result, permeability varies spatially, even at steady state. In the following, a fully coupled numerical model is developed and applied to explore the dynamics of gas flow, to numerically simulate the spatial distribution of coal permeability under various flow conditions and finally to compare the results with those from laboratory measurements.

3.1. Governing equations of coal deformation

The strain-displacement relation is defined as(Zhang et al., 2008):

$$\varepsilon_{i,j} = \frac{1}{2}(u_{i,j} + u_{j,i}) \quad (4)$$

where $\varepsilon_{i,j}$ is the component of the total strain tensor and $u_{i,j}$ is the component of the displacement. The equilibrium equation is defined as:

$$\sigma_{ij,j} + f_i = 0 \quad (5)$$

where $\sigma_{ij,j}$ is the component of total stress tensor and f_i is the component of the body force.

The permeability measurement is conducted under steady-state flow conditions when fracture-matrix interaction is in equilibrium. The coal may be represented as a uniform-pore medium with 1um radius. The coal is assumed to be a homogeneous, isotropic and elastic medium. Given that helium is non-adsorbed gas, the constitutive relations for the coal can be expressed in terms of the total stress σ_{ij} (positive for tension), strain ε_{ij}, and pore fluid pressure change p as(Detournay and Cheng, 1993):

$$\varepsilon_{ij} = \frac{1}{2G}\sigma_{ij} - \left(\frac{1}{6G} - \frac{1}{9K}\right)\sigma_{kk}\delta_{ij} + \frac{\alpha}{3K}p\delta_{ij} \quad (6)$$

where E is Young's modulus and ν is Poisson's ratio of the coal. $G = E/2(1+\nu)$ and $K = E/3(1-2\nu)$ are shear modulus and bulk modulus of the coal, respectively. α is the Biot coefficient. σ_{kk} is sum of principle stresses. The general Navier-type equation is deduced by combining Eqs. (4) to (6).

$$Gu_{i,kk} + \frac{G}{1-2\nu}u_{k,ki} - \alpha p_{f,i} + f_i = 0 \quad (7)$$

Eq. (7) is the governing equation representing mechanical deformation, where the gas pressure, can be solved from the gas flow equation.

3.2. Mass balance equation

The gas flow in the coal sample is governed by a mass balance equation (Liu et al., 2011):

$$\frac{\partial(\varphi\rho)}{\partial t} + div(\rho v) - q = 0 \tag{8}$$

where $\nu = -k/\mu \nabla p$ is the Darcy velocity, φ is coal porosity, t is time, q is gas source, and ρis gas density. Based on the ideal gas law, the gas density is defined as:

$$\rho_g = \frac{M_g}{RT} p \tag{9}$$

where ρ is gas density. M_g is molecular mass of gas. $p$is gas pressure. $R$is gas constant, and T is temperature.

Combining Eq. (8) with Eq. (9):

$$p\frac{\partial\varphi}{\partial t} + \varphi\frac{\partial p}{\partial t} + \nabla\cdot\left(-\frac{k}{\mu}\nabla p\right) - q = 0 \tag{10}$$

The coal porosity induced by coal deformation can be defined as:

$$\varphi = \varphi_0 + \Delta\varepsilon_v + \frac{\Delta p}{K_m} \tag{11}$$

where φ_0 and are initial porosity.ε_v is volumetric strain.

Based on the cubic law, the permeability is defined as a function of initial porosityk_0 and pore pressure:

$$\frac{k}{k_0} = \left(\frac{\varphi}{\varphi_0}\right)^3 = \left[1 + \frac{1}{\varphi_0}\left(\Delta\varepsilon_v + \frac{\Delta p}{K_m}\right)\right]^3 \tag{12}$$

From Eq. (12) we can see that the change in coal permeability is dominated by two parameters: coal volumetric strain, and the pore pressure change induced coal matrix compaction.

3.3. Flow regime transition

The constant confining pressure applied to the sample, combined with a varying pressure along the sample, results in a non-uniform effective stress along the flow direction. This downstream-increasing effective stress decreases mean pore size and may prompt the evolution of transitional flow regimes. The exponential expression derived from the Klinkenberg model (Klinkenberg, 1941a) has been used to determine the fluid-dynamic effect and poro-elastic effect individually on permeability change. However, the Klinkenberg-model-based exponential expression is only applicable to first-order slip flow without considering the transition in the flow regime. The Knudsen number has been widely adopted to classify dominant flow mechanisms (Bird, 2003):

$$K_n = \frac{\lambda}{d} \tag{13}$$

where λ (m) is the mean free path length and d (m) is the transport pore diameter, equal to the mean radius of the pore throat. The mean pore throat diameter selected in the model is 1.0 μm, which is treated as an equivalent pore radius for calculation of the Knudsen number. A general relationship between Knudsen number and the apparent permeability multiplier may be defined as (Beskok and Karniadakis, 1999):

$$\mathrm{k_{app}} = \mathrm{k_{int}}(1 + \gamma \mathrm{K_n})\left(1 + \frac{4\mathrm{K_n}}{1 + \mathrm{K_n}}\right) \tag{14}$$

where $\mathrm{k_{int}}$ is intrinsic permeability, $\mathrm{K_n}$ is Knudsen number and $\gamma = 128/15\pi^2 \cdot \tan^{-1}(4\mathrm{K_n}^{0.4})$ is the Boltzmann constant.

As previously presented in Section 2.2, the application of confining pressure on the coal sample compacts the bulk coal and may compact some macro cleats. Moreover, it can be speculated from the observed enhancement in permeability at low pressure, as shown in Fig. 4, that the diameter of the gas flow conduit is sufficiently narrowed to be comparable with the mean free path of the helium molecules. In this work, therefore, the complex pore structure of coal is simplified into a uni-pore medium, according to pore size distribution of Fig. 2. To calculate the Knudsen number, two assumptions are made here: (i) the external stress and the injection gas pressure result only in elastic deformation, and (ii) the pore diameter responds elastically to this variable effective stress while the total number of pores in the sample remain unchanged. For any cross section of the coal sample (perpendicular to the gas flow direction), the total number of pores,n, can be described as:

$$\mathrm{n} = \frac{\varphi_0}{\pi \mathrm{r}_0^2}\mathrm{A}_0 = \frac{\varphi}{\pi \mathrm{r}^2}\mathrm{A} \tag{15}$$

where the subscript, 0, is the initial value of the variable, A is the cross-sectional area of the coal sample, r is mean radius of the pores and φ is porosity.

According to Eq. (15), the mean radius of the pores can be expressed as a function of coal strain, $\Delta\varepsilon_v$ and porosity, φ, as:

$$r = r_0\sqrt{\frac{\phi}{\phi_0}\frac{A}{A_0}} = r_0\sqrt{\frac{\phi}{\phi_0}(1 + \Delta\varepsilon_v)} \tag{16}$$

The Knudsen number is ratio of the mean free path of the gas λ to pore size r:

$$K_n = \frac{\lambda}{2r} = \frac{\frac{\mu}{p}\cdot\sqrt{\frac{\pi ZRT}{2M_g}}}{2r} \tag{17}$$

Eqs. (16) and (17) may be substituted into Eq. (14) to calculate the dynamic change in permeability during the flow process.

3.4. Model implementation and validation

The permeability sample is simplified into a 2D symmetric model, as shown in Fig. 6. The sample is represented as a prism 50 mm × 25 mm (length by height) with the left and right ends constrained laterally by roller boundaries with the upper and lower boundaries constrained by constant stress – this replicates the laboratory conditions. Non-absorbing gas (helium) is injected (right) and recovered (left) at prescribed pressure. The initial gas pressures are as noted in Fig. 4 with outlet pressure at atmospheric (101 kPa). Zero flux is specified on the upper and lower boundaries of the model. The field equations are implemented and solved using COMSOL Multiphysics. Relevant initial values of parameters are listed in Table 3.

Two separate confining pressures (8 MPa then 12 MPa) are separately applied with gas pressure subsequently applied following the steps illustrated in Fig. 4. Simulated gas outflow rates are compared with the experimental results for the same flow conditions in Fig. 7. Results show that the modeling outflow rates are in good agreement with the directly measured flow rates.

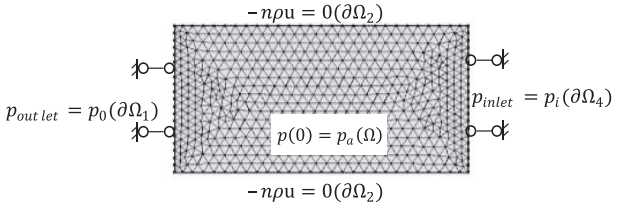

Fig. 6. Geometry of the 2D symmetric model together with initial and boundary conditions.

Table 3
Modeling parameters used in the numerical analysis.

Symbol	Value	Parameter	Unit
E	3766	Young's module	MPa
μ	0.38	Poisson ratio	–
N	1.84×10^{-5}	Gas dynamic viscosity	Pa·s
ϕ_{f0}	2.5	Initial cleat porosity	%
k_{f0}	6.8×10^{-18}	Initial cleat permeability	m^2
P_0	0.1	Outlet pressure	MPa
P_{con}	8/12	Confining stress	MPa
ρ_c	1250	Coal density	kg/m^3
p_a	0.1	Atmospheric pressure	MPa
A	1	Shape factor	m^{-2}
r_0	1×10^{-6}	Initial pore radius	m
α	0.2	Biot's coefficient	-

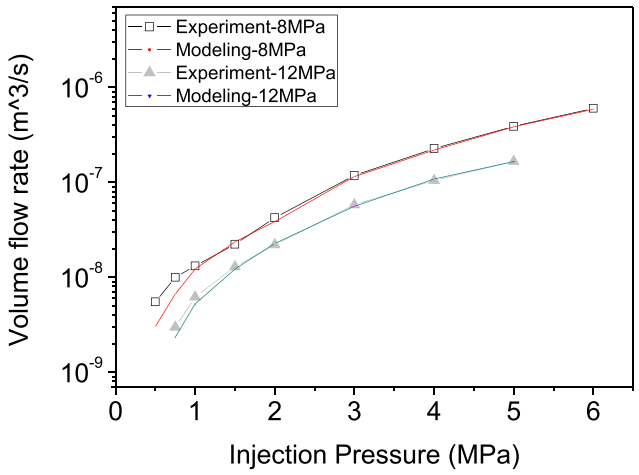

Fig. 7. Comparison of numerical and experimental results of outflow rate.

4. Analysis of gas flow behavior

Various gas-coal interaction parameters along the flow pathway, including pore pressure, Knudsen number and intrinsic/apparent permeability ratios are extracted from the numerical model. Figs.8 and 9 show the modeling results at equilibrium flow condition for confining stresses of 8 MPa and 12 MPa, respectively.

4.1. Flow regime transition and permeability features

Figs.8a and 9a show the distribution of pore pressure along the gas flow direction. The pore pressure shows a clear nonlinear distribution along the flow direction, and the pressure gradient increases gradually towards the gas outlet – due to the compressible nature of the (helium) gas (Liu et al., 2015; Liu et al., 2017). The intrinsic permeability ratio reduces downstream (towards the outlet), but for the same location, a smaller permeability ratio is observed when injection pressure is greater, as shown in Fig. 8b and Fig. 9b.

As noted previously, the magnitude of the pore pressure in the coal sample may not only change the mean molecular free path of the helium, but also influence the gas dynamics in the flow channels. Knudsen numbers increase significantly in the vicinity of the outlet (lower pressure region), as illustrated in Figs. 8c and 9c, indicating a transition in flow regime within the sample.

In this study, we adopt the conventional criterion discriminating flow regime and define a Knudsen number of 0.01 as the threshold separating slip flow from viscous flow - although some debate exists regarding this threshold value. Apparent from Fig. 8b and Fig. 9b is that for injection pressures below 1 MPa, the Knudsen number across the entire coal sample is in excess of 0.01 but < 0.1, indicating that gas

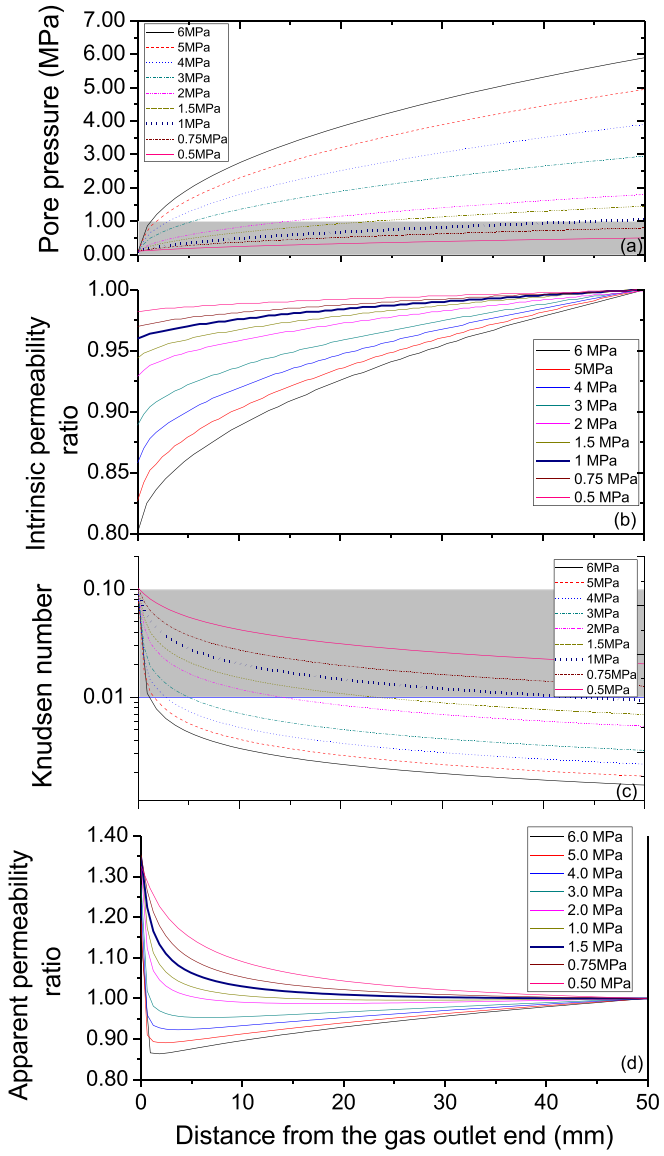

Fig. 8. Steady-state flow of helium in the coal sample under 8 MPa confining pressure. Grey shaded area is slip flow: (a) Pore pressure distribution; (b) Intrinsic permeability ratio; (c) Knudsen number; and (d) Apparent permeability ratio.

slippage is expected to occur in the entire coal sample. The associated apparent permeability ratio increases monotonically along the gas flow direction. This phenomenon may illustrated by Klinkenberg plots (Feng et al., 2017), in which apparent permeability follows a near linear relationship with reciprocal mean gas pressure < 1/MPa.

For the cases where the injection pressure is higher than 1 MPa, the apparent permeability ratios are observed to evolve from reduction to enhancement, as shown in Fig. 8d and Fig. 9d. For this coal sample, the minimum apparent permeability occurs consistently at a critical mean pore pressure of 1.0 MPa. The corresponding location of this mean pore pressure marks the boundary separating the poroelastic dominant region and the fluid-dynamics dominant region. Gas flow along the coal sample can therefore be divided into two regimes: a gas slippage regime (the Knudsen number range between 0.01 and 0.1) and a viscous flow regime (i.e. Kn < 0.01), as shown in Fig. 10.

In the following, the equivalent apparent permeability for each flow regime is calculated and compared with the overall apparent permeability of the sample. In view of the steady state flow for each injection pressure at equilibrium, the mass flux rate of gas at any cross-section of

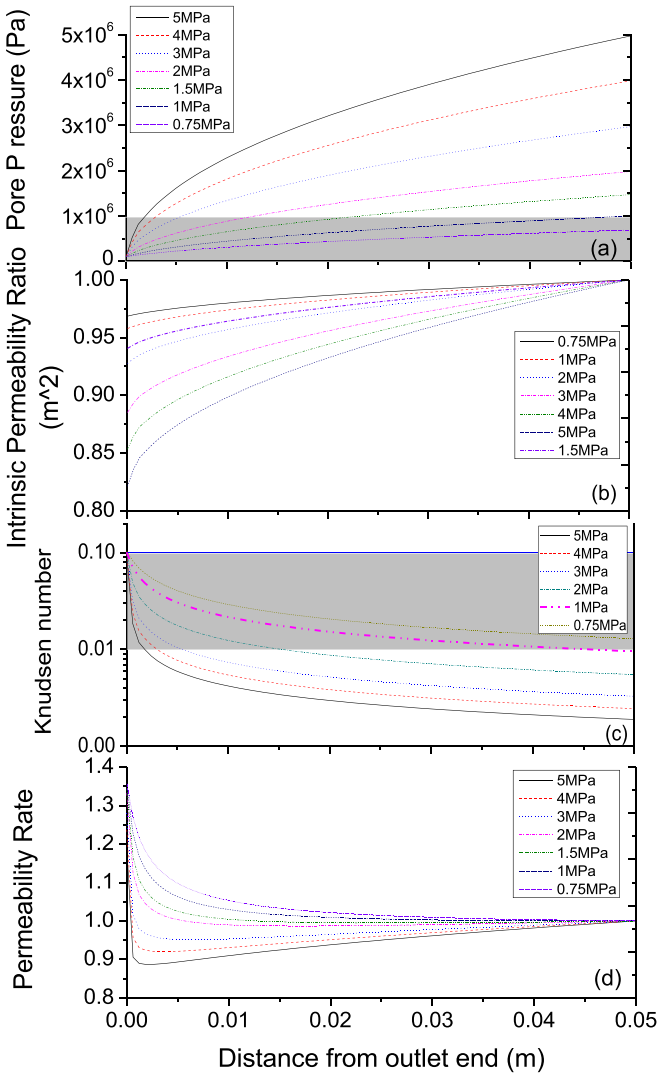

Fig. 9. Steady-state flow of helium in the coal sample under 12 MPa confining pressure. Grey shaded area is slip flow: (a) Pore pressure distribution; (b) Intrinsic permeability ratio; (c) Knudsen number; and (d) Apparent permeability ratio.

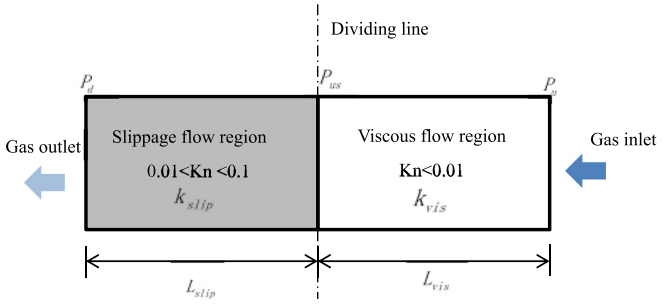

Fig. 10. Schematic diagram of distribution of gas flow regimes in a coal sample.

the coal sample is equal to the gas mass flux rate at the outlet. Thus, the permeability of the slip flow and viscous flow regions can be determined from Eq. (18) and Eq. (19), respectively.

$$k_{vis} = -\frac{2\dot{m}\cdot\mu\cdot L_{vis}\cdot P_{us}}{A\cdot(P_{us}^2 - P_u^2)\rho_{vis}} \text{ for the viscous flow region} \quad (18)$$

$$k_{slip} = -\frac{2\dot{m}\cdot\mu\cdot L_{slip}\cdot P_d}{A\cdot(P_d^2 - P_{us}^2)\rho_{out}} \text{ for the slip flow region} \quad (19)$$

The overall apparent permeability can be calculated using Eq. (20).

$$k_{app} = -\frac{2\dot{m}\cdot\mu\cdot L\cdot P_u}{A\cdot(P_d^2 - P_u^2)\rho_{out}} \text{ for the overall sample} \quad (20)$$

where k_{vis} is the apparent permeability of the viscous flow region, $\dot{m}$ is the gas mass flux rate, $k_{slip}$is the apparent permeability of the slip flow region, and k_{app} is the apparent permeability of the global flow region. L_{vis} is the length of the viscous flow region, and L_{slip} is the length of the slip flow region. ρ_{out} is the outlet gas density and ρ_{vis} denotes the gas density on the dividing line between viscous flow and slip flow regimes. P_{us} denotes the critical pore pressure that divides the viscous flow region and slip flow region. In this work, the critical pore pressure P_{us} is calculated as 1 MPa.

Quantifying the response of the gas slip flow regime to injection pressure is important for a better understanding of the evolution of apparent permeability. Fig. 8a and Fig. 9a show that the length of the slip flow region (L_{slip}) increases with a reduction in the injection pressure. To better quantify the change in L_{slip}, we introduce a term denoted as the "Length Ratio", defined as the length of slip flow region (L_{slip}) to the total length of the coal sample ($L_{slip} + L_{slip}$). The results are plotted in Fig. 11, showing that both length ratios, for both confining pressure conditions, decay gradually with an increase in the injection pressure. No significant difference in the values of the ratio are observed for the same injection pressure, despite the applied confining pressure values being different. The consistency between the two length-ratio curves (shown in Fig. 11) reflects the spatial change of the threshold value of the pore pressure within the coal sample. This is largely determined by the pressure injection conditions and the flow length. For the coal sample, the pore pressure distribution is predominately determined by upstream injection pressure.

To compare the differences in the equivalent apparent permeability for each flow regime, the apparent permeability values for confining stresses of 8 MPa and 12 MPa are calculated using Eqs. (18)–(20) and plotted in Fig. 12a and Fig. 12b, respectively. Results show that the values of the equivalent apparent permeability in both the slip flow and the viscous flow regions are close to the respective measured permeabilities. The permeability of the slip flow region gives the highest value, followed by the overall permeability followed by the slip flow permeability.

The two flow regimes occur concurrently in each flow region, suggesting that viscous flow still exerts a dominant effect. In order to quantify the contribution of the slip effect in the slip flow region to the total flow, the term 'Gas Flux ratio' is introduced - this is defined as the ratio of the slip flow rate to viscous flow rate. In this work, the viscous

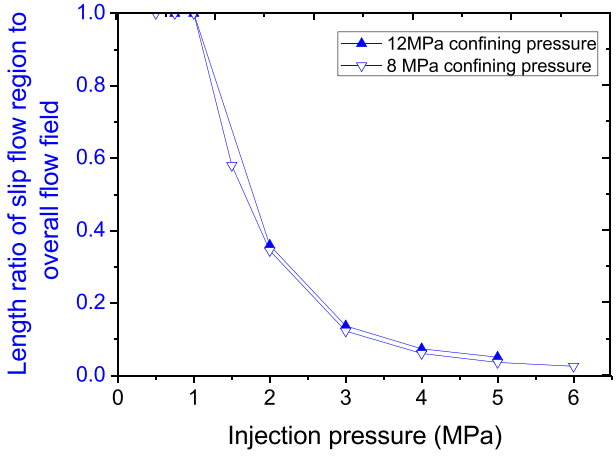

Fig. 11. Change in the length ratio with respect to different injection pressures.

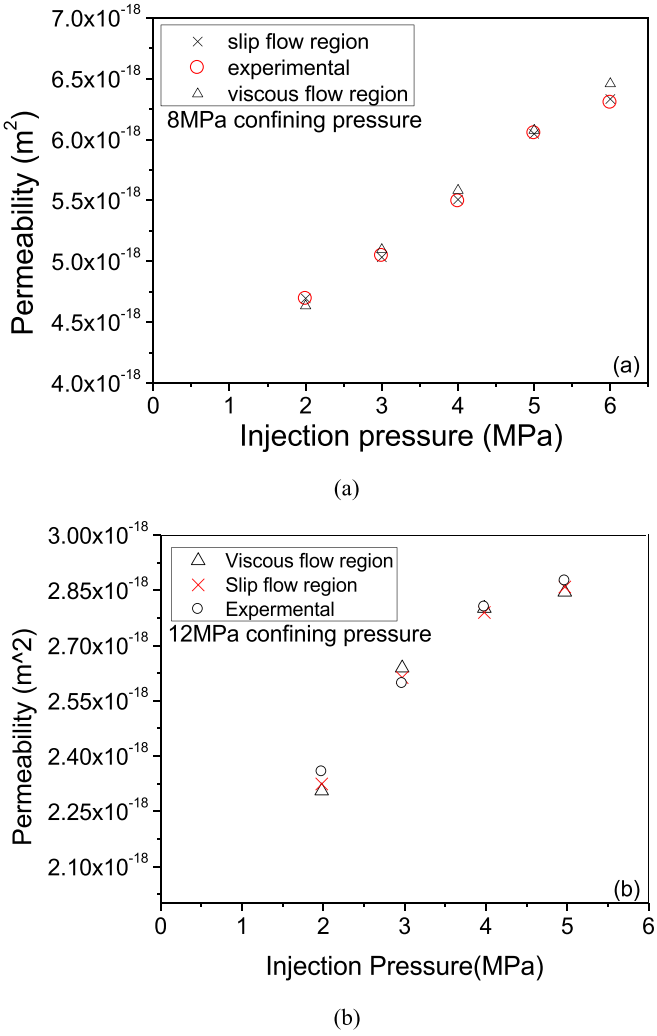

Fig. 12. Comparison of the apparent permeability of the viscous flow and slippage flow regions with the overall apparent permeability under two separate confining stresses of: (a) 8 MPa, and (b) 12 MPa.

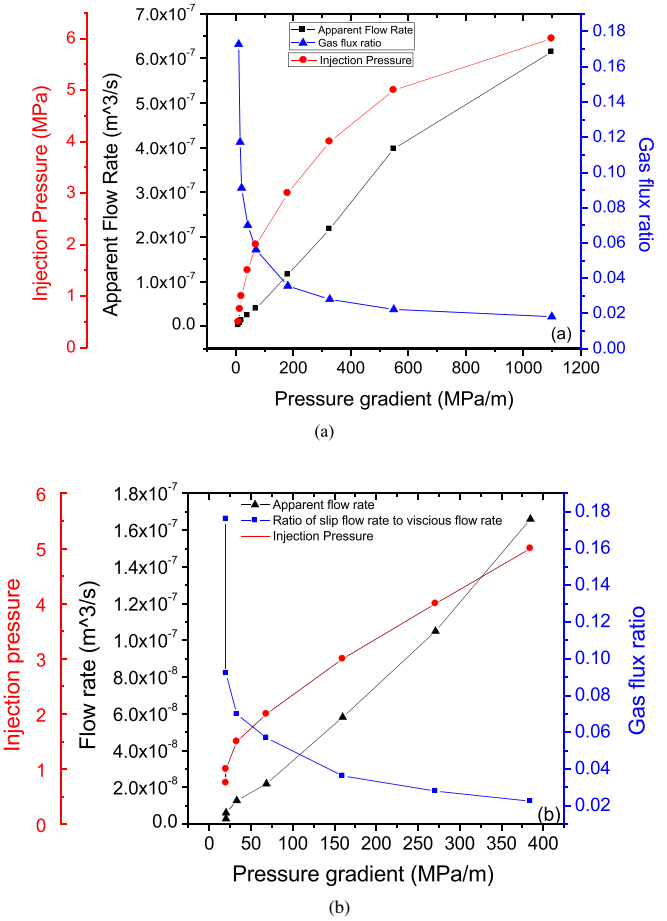

Fig. 13. Response of the Gas Flux ratio and the apparent flow rate to the pressure gradients within the slip flow region for two different confining stresses of: (a) 8 MPa, and (b) 12 MPa.

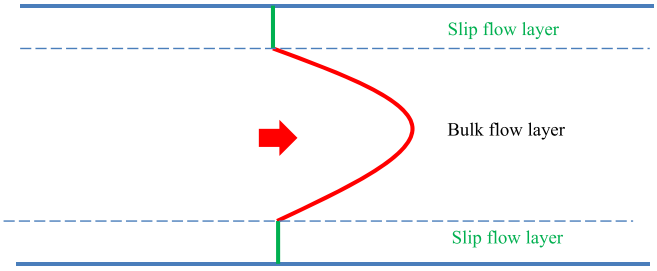

Fig. 14. Conceptual velocity profile across a micro-channel. The red curve represents the bulk flow layer where the wall barely impacts the flow. The green lines inside the Knudsen flow layer indicate the average velocity of the Knudsen layer (Present, 1958; Wang et al., 2016c). (For interpretation of the references to colour in this figure legend, the reader is referred to the web version of this article.)

flow rate is obtained from the numerical simulation results and the slip flow rate is calculated as the difference between the apparent flow rate in this region (measured flow rate) and the viscous flow rate.

As shown in Fig. 13a and b, the apparent flow rate drops as the injection pressure decreases. Meanwhile, the Gas Flux ratio increases considerably from 0.02 to 0.18. This indicates that the mass transport of gas in the coal sample is predominately driven by the pressure gradient - the actual contribution of the slip flow to the total flow can be significantly different. The ratio increases exponentially with a drop in gas injection pressure. This phenomenon can be explained with the concept of velocity profile (Karniadakis et al., 2005; Wang et al., 2016b), in which the total gas flux can be approximately divided into the slip flow layer and the bulk flow layer (Fig. 14). Although fluid viscosity can push the viscous flow boundary close to the walls of the flow channel, the gas molecules are in motion at the wall interface, and these lubricate the flow boundary and contribute to the additional flux.

These findings indicate that the pressure-gradient-driven gas flow complicates the gas flow regime as well as the distribution of the apparent permeability within the sample. In this work, the critical pore pressure of 1 MPa is an upper threshold pressure defining the slip flow regime for a sample with mean pore size of 1 μm. According to the definition of the Knudsen number (Eq. (17)), changes in the upper threshold pressure for slip flow with respect to mean pore size, are plotted in Fig. 15. Results show that the upper threshold pressure for slip flow increases with a decrease in pore size. When pore size is fixed, the gas flow regime can transit from slip flow to viscous flow with increasing pore pressure. If pore pressure is held constant, the gas flow regime can also change from viscous flow to slip flow with decreasing pore radius. This trend explains why ultra-low permeability rocks exhibit slippage effects, even under high pore pressure flow conditions. In order to directly measure non-slip gas permeability under steady-state flow, several researchers have applied a finite backpressure at the downstream end of the sample (Rushing et al., 2004; Dong et al., 2012; Li et al., 2009b). Then, selecting an approximate pressure is critical to effectively minimize non-Darcy effects. From this work, the upper threshold pressure can act as a minimum backpressure, whose magnitude is closely related with size of pores carrying gas.

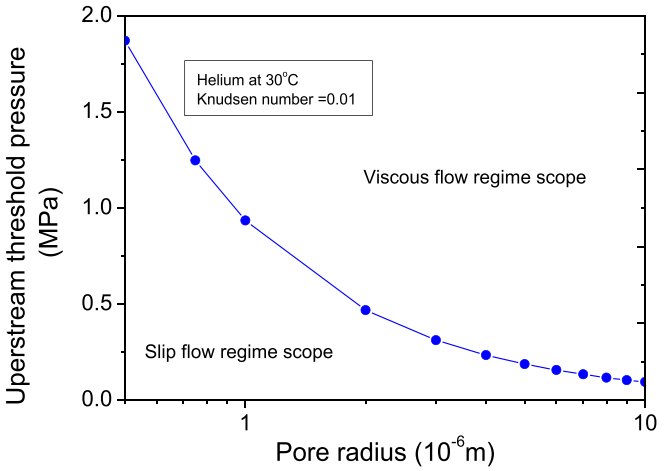

Fig. 15. Magnitude of the upper threshold pressure for slip flow as a function of pore radii in the range 50 nm to 10 μm.

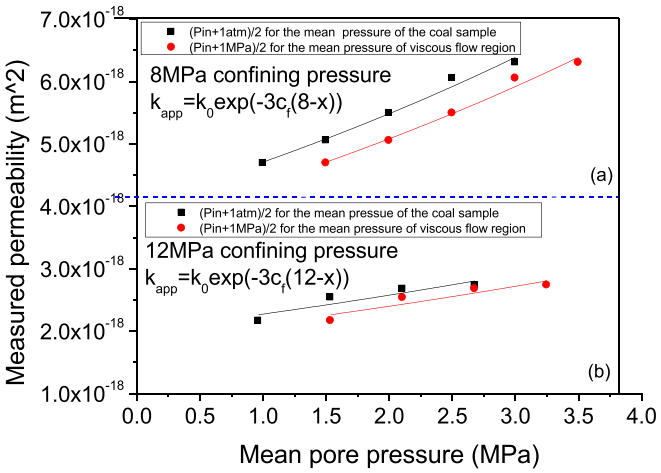

Fig. 16. Measured permeability vs the mean pressure of the coal sample, or of the viscous flow region.

4.2. Comparison of permeability-pressure relations

Permeability is a measure of how readily a fluid can flow through a porous material under a differential pressure. When plotting permeability values against pore pressure, the selection of the appropriate and representative pore pressure is critically important for accurate determination of the intrinsic permeability. Otherwise, the features of permeability evolution may be misrepresented. This in turn may result in an inaccurate prediction of gas production when conducting reservoir simulation at field scale. As mentioned, for the steady-state method, the measured permeability magnitude is typically plotted against the mean pressure, calculated as the average of inlet and outlet pressures. In the following, two alternate methods of defining this permeability-pressure relation are introduced. These are: (i) measured permeability vs. mean pore pressure of the viscous flow regime, and (ii) modelled permeability vs. the mean pressure of the inlet and outlet pressures. The differences in permeability magnitudes for the same pore pressure among the three methods are compared separately and analyzed in detail.

For method (i), the mean pore pressure of the viscous flow region is defined as the mean value of the injection pressure plus the upstream pressure of the slip flow region (i.e., 1 MPa for this coal sample). The results are compared with the permeability values calculated in the conventional way. A constant compressibility is used in fitting the data. Parameter fitting of an exponential permeability function is also conducted for both confining stresses, and the fitted parameter values listed in Table 4. A comparison of the permeability-pressure relation is shown in Fig. 16. The fitted intrinsic permeability values derived from 1 MPa downstream pressure are lower than the Klinkenberg-corrected permeabilities with 1 atm downstream pressure, as listed in Table 3. These findings are consistent with experimental observations by Li et al., 2009a and Dong et al., 2012. The discrepancy is attributable to the nonlinear extrapolation of curve of permeability -versus- the reciprocal of pressure. Besides, the commonly used approach defines a higher permeability value than approach (i). The differences are 7.66% and 7.45% for 8 MPa and 12 MPa, respectively.

For method (ii), the value of the modelled permeability is obtained from numerical model at the cross-section of the sample where the pore pressure is the mean of inlet and outlet pressures (i.e., the mean pore pressure used in the conventional data plotting for the steady-state method). Comparisons of the results between the conventional approach and the approach (ii) are shown in Fig. 17a, b. Results demonstrate that for the tested sample, when pressure is low (i.e. 1.0 MPa), the difference in measured permeability between the two methods is negligible - with the modelled permeability giving slightly higher value. However, the opposite is observed for conditions of high injection pressures, where measured permeabilities are always greater than the modelled values. We use Eq. (21) to evaluate the difference between modelled and measured permeability, as,

$$\text{Difference} = \frac{k_{\text{modelled}} - k_{\text{measured}}}{k_{\text{measured}}} \times 100\% \quad (21)$$

where k_{modelled} is modelled permeability and k_{measured} is measured permeability. Fig. 17c shows that this difference increases rapidly with pore pressure and is as high as 4.8% at a mean pore pressure of 3.0 MPa. The difference is expected to be even higher for greater injection pressure values. These results clearly indicate that the choice of measuring and calculating coal permeability using the steady-state flow method may result in a certain degree of data uncertainty, and thus an appropriate sensitivity analysis is desired when injection pressure is high or when samples have very low permeability.

5. Conclusions

Measurements of coal permeability to helium are integrated with numerical modeling to investigate the distribution of the features of viscous and slip regimes of flow within a tight coal sample. These observations are used to analyze the potential uncertainty associated with permeability estimations when using steady-state flow methods. The main conclusions are as follows:

(1) Viscous flow and slip flow regimes may occur concurrently within a

Table 4
Comparison of fitting parameters using different definitions of "mean" pressures.

	Confining pressure = 8 MPa	Confining pressure = 12 MPa
Intrinsic permeability, k_0, m^2 (using the mean pressure of the entire coal sample)	1.37×10^{-17}	1.0919×10^{-17}
Stress coefficient, c_f, 1/MPa	0.0508	0.0478
Intrinsic permeability, k_0, m^2 (using the mean pressure of the viscous flow region)	1.27×10^{-17}	1.0163×10^{-17}
Compressibility, c_f, 1/MPa	0.0508	0.0478

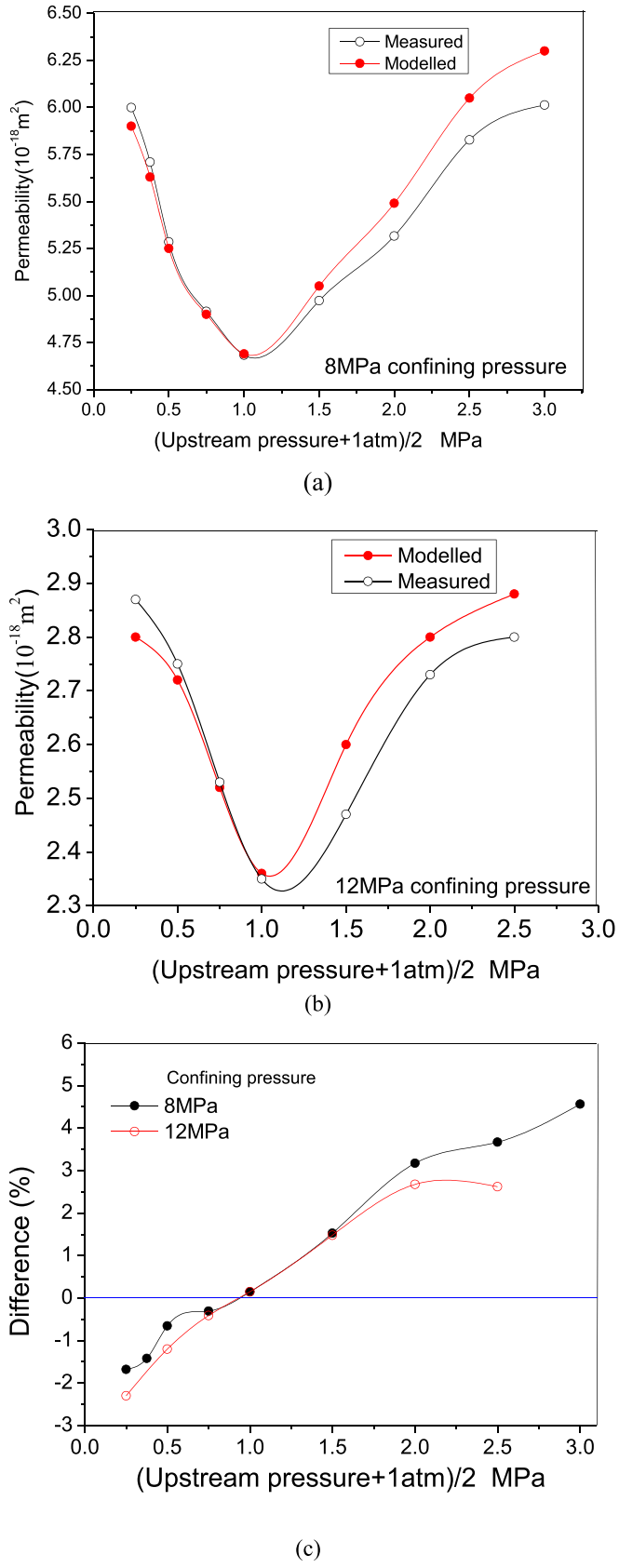

Fig. 17. Measured permeability vs mean pressure of the coal sample for confining stresses of: (a) 8 MPa; (b) 12 MPa, and (c) The difference in permeability values.

sample when pore pressure is higher than 1.0 MPa. The length of the slip dominant flow region increases exponentially with increasing effective stress. The flow becomes (completely) slip dominant when the mean pressure drops to 1.0 MPa or below. The specific contribution of the slip flow to total flow enhances with the reduction in pore pressure, increasing from 0.02 to 0.18.

(2) For the tested sample, the equivalent permeability for both viscous and slip flow regimes is very close to the actual measured permeability.

(3) Compared with the two newly proposed alternative methods, the conventional way of calculating the apparent permeability, using the steady-state flow method, always returns a greater permeability value, by up to 7.66%. This difference is expected to increase at higher injection pressures. Hence, an uncertainty analysis is strongly recommended when using this experimental method to measure permeability change with pore pressure.

The findings and methodology developed in this work are expected to benefit many applications (e.g. from unconventional gas extraction, to CO_2 sequestration, and to geothermal recovery) via the improvement in the confidence of decision making.

Acknowledgement

The financial support from the National Natural Science Foundation of China (No. 41772154), China Postdoctoral Science Foundation (2018T110816), Natural Science Foundation of Shandong Province (ZR2017MEE003, ZR2019MA009), and SDUST Research Fund (2018TDJH102) are all gratefully acknowledged. The authors are also grateful to Mr. Licai Zheng from Sanying Precision Instruments *Co.*, Ltd.

Appendix

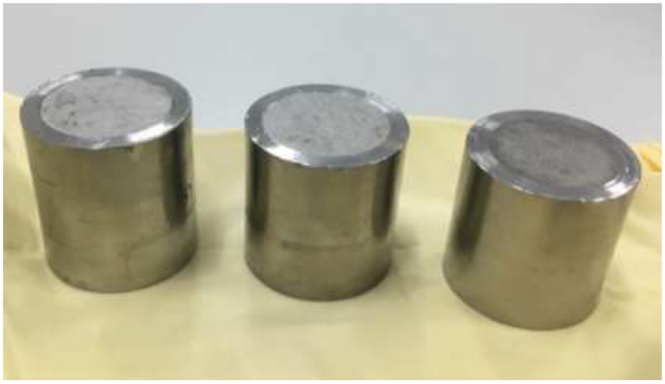

Fig. A1. Photos of the three standard samples used to calibration the experimental apparatus. From left to right: No1 sample (SY-10011), No2 sample (SY-10011) and No3 sample (SY-10011).

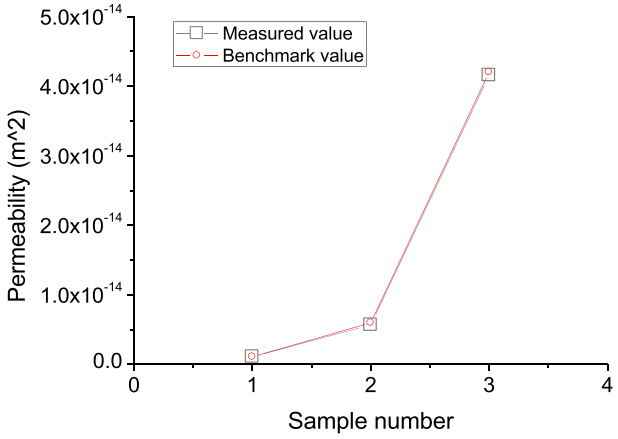

Fig. A2. Comparison of permeability values measured in the lab and standard value.

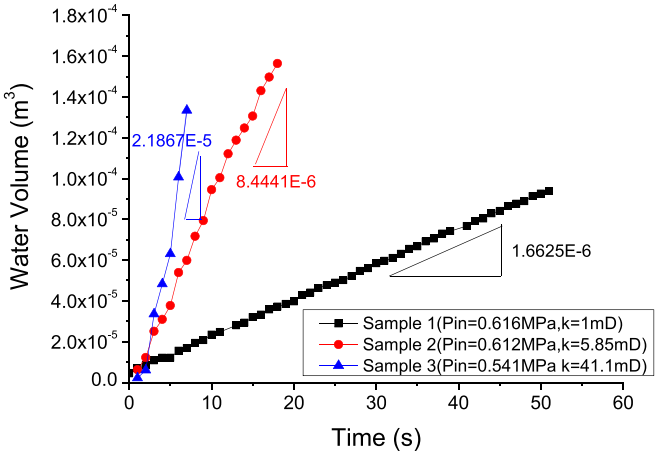

Fig. A3. Evolution of water weight for the three standard sample.

Table A1
Experimental pressure parameter.

Sample number	Inlet pressure (MPa)	Outlet pressure (MPa)	Flow rate ($\times 10^{-6}$ m^3/s)	Measured permeability ($\times 10^{-15}$ m^2)	Benchmark permeability ($\times 10^{-15}$ m^2)
SY-10011	0.616	0.008	1.6625	1.00378	1.07
SY-10012	0.612	0.028	8.4440	5.84983	5.97
SY-10013	0.547	0.136	21.867	41.1166	42.0

References

Amann-Hildenbrand, A., Ghanizadeh, A., Krooss, B.M., 2012. Transport properties of unconventional gas systems. Mar. Petrol. Geol. 31, 90–99.

Anggara, F., Sasaki, K., Sugai, Y., 2016. The correlation between coal swelling and permeability during CO 2 sequestration: a case study using Kushiro low rank coals. Int. J. Coal Geol. 166, 62–70.

Beskok, A., Karniadakis, G.E., 1999. A model for flows in channels, pipes, and ducts at micro and nano scales. Microscale Thermophys. Eng. 3 (1), 43–77.

Bird, G.A., 2003. Molecular Gas Dynamics and the Direct Simulation of Gas Flows. Oxford University Press Inc, New York.

Bourbie, T., Walls, J., 1982. Pulse decay permeability:analytical solution and experimental test. SPE J. 22, 719–722.

Brace, W.F., Walsh, J.B., Frangos, W.T., 1968a. Permeability of granite under high pressure. J. Geophys. Res. 73 (6), 2225–2236.

Brace, W.F., Walsh, J.B., Frangos, W.T., 1968b. Permeability of granite under high pressure. J. Geophys. Res. 73 (6), 2225–2236.

Chen, G., 1994a. Gas Slippage and Matrix Shrinkage Effects on Permeability of Coal. The University of Arizona, USA (PhD thesis).

Chen, G., 1994b. Gas Slippage and Matrix Shrinkage Effects on Permeability of Coal. The University of Arizona, USA (PhD thesis).

Chen, Z., Pan, Z., Liu, J., Connell, L.D., Elsworth, D., 2011. Effect of the effective stress coefficient and sorption-induced strain on the evolution of coal permeability: experimental observations. Int. J. Greenh Gas Control 5 (5), 1284–1293.

Civan, F., 2010. Effective correlation of apparent gas permeability in tight porous media. Transp. Porous Media 82, 375–384.

Cui, X., Bustin, R.M., 2005. Volumetric strain associated with methane desorption and its impact on coalbed gas production from deep coal seams. AAPG Bull. 89 (9), 1181–1202.

Cui, Guanglei, Liu, Jishan, Wei, Mingyao, Shi, Rui, Elsworth, D., 2018. Why shale permeability changes under variable effective stresses: new insights. Fuel 213, 55–71.

Detournay, E., Cheng, A.H.D., 1993. Fundamentals of poroelasticity. In: Fairhurst, C. (Ed.), Comprehensive Rock Engineering. vol. 2. Pergamon, Oxford, pp. 113–171.

Dong, M., Li, Z., Li, S., Yao, J., 2012. Permeabilities of tight reservoir cores determined for gaseous and liquid CO2 and C_2H_6 using minimum backpressure method. J. Nat. Gas Sci. Eng. 5, 1–5.

Fan, K., Dong, M., Elsworth, D., et al., 2018. A dynamic-pulse pseudo-pressure method to determine shale matrix permeability at representative reservoir conditions[J]. Int. J. Coal Geol. 193, 61–72.

Feng, R., Harpalani, S., Pandey, R., 2017. Evaluation of various pulse-decay laboratory permeability measurement techniques for highly stressed coals. Rock Mech. Rock. Eng. 50 (2), 297–308.

Fink, Reinhard, Krooss, Bernhard M., Gensterblum, Yves, Amann-Hildenbrand, Alexandra, 2017. Apparent permeability of gas shales-Superposition of fluid-dynamic and poro-elastic effects. Fuel 199, 532–550.

Gasparik, M., Ghanizadeh, A., Bertier, P., Gensterblum, Y., Krooss, B.M., Littke, R., 2013. Geological controls on the methane storage capacity in organic-rich shales. Int. J. Coal Geol. 123 (2), 34–51.

Gasparik, M., Bertier, P., Gensterblum, Y., Ghanizadeh, A., Krooss, B.M., Littke, R., 2014.

Geological controls on the methane storage capacity in organic-rich shales. Int. J. Coal Geol. 123 (2), 34–51.
Gensterblum, Y., Ghanizadeh, A., Krooss, B.M., 2014a. Gas permeability measurements on Australian subbituminous coals: fluid dynamic and poroelastic aspects. J. Nat. Gas Sci. Eng. 19, 202–214.
Gensterblum, Y., Ghanizadeh, A., Krooss, B.M., 2014b. Gas permeability measurements on Australian subbituminous coals: fluid dynamic and poroelastic aspects. J. Nat. Gas Sci. Eng. 19, 202–214.
Gray, I., 1987. Reservoir engineering in coal seams: Part 1. 1987. The physical process of gas storage and movement in coal seams. SPE Reserv. Eng. 2 (01), 28–34.
Han, F., Busch, A., Krooss, B.M., Liu, Z., van Wageningen, N., Yang, J., 2010. Experimental study on fluid transport processes in the cleat and matrix systems of coal. Energy Fuel 24 (12), 6653–6661.
Harpalani, S., Chen, G., 1997a. Influence of gas production induced volumetric strain on permeability of coal. Geotech. Geol. Eng. 15 (4), 303–325.
Harpalani, S., Chen, G., 1997b. Influence of gas production induced volumetric strain on permeability of coal. Geotech. Geol. Eng. 15, 303–325.
Harpalani, S., Schraufnagel, R.A., 1990. Shrinkage of coal matrix with release of gas and its impact on permeability of coal. Fuel 69 (5), 551–556.
Heller, R., Vermylen, J., Zoback, M., 2014a. Experimental investigation of matrix permeability of gas shales. AAPG Bull. 98, 975–995.
Heller, R., Vermylen, J., Zoback, M., 2014b. Experimental investigation of matrix permeability of gas shales. AAPG Bull. 98, 975–995.
Hsieh, P.A., Tracy, J.V., Neuzil, C.E., Bredehoeft, J.D., Silliman, S.E., 1981. A transient laboratory method for determining the hydraulic properties of tight rocks-I. Theory. Int. J. Rock Mech. Min. Sci. Geomech. AOthersbstracts 18 (3), 245–252.
Jones, C., Meredith, P., 1998. An experimental study of elastic propagation anisotropy and permeability anisotropy in an illitic shale. In: Presented at the SPE/ISRM Eurock, Trondheim, Norway, 8–10 July.
Karniadakis, G., Beskok, A., Aluru, N., 2005. Microflows and Nanoflows: Fundamentals and Simulation. Springer Science & Business Media.
Klinkenberg, L.J., 1941a. The Permeability of Porous Media to Liquids and Gases. Presented at the Drilling and Production Practice. American Petroleum Institute.
Klinkenberg, L., 1941b. The permeability of porous media to liquids and gases. In: Drilling and Production Practice. American Petroleum Institute.
Kumar, H., Elsworth, D., Mathews, J.P., Marone, C., 2016. Permeability evolution in sorbing media:analogies between organic-rich shale and coal. Geofluids 16 (1), 43–55.
Laubach, S.E., Marrett, R.A., Olson, J.E., Scott, A.R., 1998. Characteristics and origins of coal cleat: a review. Int. J. Coal Geol. 35 (1), 175–207.
Li, S., Dong, M., Li, Z., 2009a. Measurement and revised interpretation of gas flow behaviour in tight reservoir cores. J. Petrol. Sci. Eng. 65, 81–88.
Li, S., Dong, M., Li, Z., 2009b. Measurement and revised interpretation of gas flow behaviour in tight reservoir cores. J. Petrol. Sci. Eng. 65, 81–88.
Li, J., Liu, D., Yao, Y., Cai, Y., Chen, Y., 2013. Evaluation and modeling of gas permeability changes in anthracite coals. Fuel 111, 606–612.
Liu, J., Chen, Z., Elsworth, D., Qu, H., Chen, D., 2011. Interactions of multiple processes during cbm extraction: a critical review. Int. J. Coal Geol. 87 (3–4), 175–189.
Liu, Q., Cheng, Y., Zhou, H., Guo, P., An, F., Chen, H., 2015. A mathematical model of coupled gas flow and coal deformation with gas diffusion and klinkenberg effects. Rock Mech. Rock Eng. 48 (3), 1163–1180.
Liu, T., Lin, B., Yang, W., Zhai, C., Liu, T., 2017. Coal permeability evolution and gas migration under non-equilibrium state. Transp. Porous Media 118 (1), 1–24.
Malkovsky, V.I., Zharikov, A.V., Shmonov, V.M., 2009. New methods for measuring the permeability of rock samples for a single- phase fluid. Izvestiya. Phys. Solid Earth 45 (2), 89–100.
Meng, Y., Li, Z., 2017. Triaxial experiments on adsorption deformation and permeability of different sorbing gases in anthracite coal. J. Nat. Gas Sci. Eng. 46, 59–70.
Pan, Z., Connell, L.D., 2012. Modelling permeability for coal reservoirs: a review of analytical models and testing data. Int. J. Coal Geol. 92, 1–44.
Pan, Z., Connell, L.D., 2015. Reservoir simulation of free and adsorbed gas production from shale. J. Nat. Gas Sci. Eng. 22, 359–370.
Pan, Z., Connell, L.D., Camilleri, M., 2010. Laboratory characterisation of coal reservoir permeability for primary and enhanced coalbed methane recovery. Int. J. Coal Geol. 82 (3), 252–261.
Pattison, C.I., Fielding, C.R., McWatters, R.H., Hamilton, L.H., 1996. Nature and origin of fractures in Permian coals from the Bowen Basin, Queensland, Australia. Geol. Soc. Lond. Spec. Publ. 109 (1), 133–150.
Pini, R., Ottiger, S., Burlini, L., Storti, G., Mazzotti, M., 2009. Role of adsorption and swelling on the dynamics of gas injection in coal. J. Geophys. Res. 114 (B4).
Present, R.D., 1958. Kinatic Theory of Gases.
Robertson, E.P., Christiansen, R.L., 2005. Modeling Permeability in Coal Using Sorption-Induced Strain Data. Idaho National Laboratory (INL).
Rui, Shi, Jishan, Liu, Mingyao, Wei, Derek, Elsworth, Xiaoming, Wang, 2018. Mechanistic analysis of coal permeability evolution data under stresscontrolled conditions. Int. J. Rock Mech. Min. Sci. 110, 36–47.
Rushing, J.A., Newsham, K.E., Lasswell, P.M., Cox, J.C., Blasingame, T.A., 2004. Klinkenberg-corrected permeability measurements in tight gas sands: Steadystate versus unsteady-state techniques. In: Presented at the SPE Annual Technical Conference and Exhibition in Houston, Texas, 26e29 September.
Seomoon, H., Lee, M., Sung, W., 2015. Analysis of sorption-induced permeability reduction considering gas diffusion phenomenon in coal seam reservoir. Transp. Porous Media 108 (3), 713–729.
Shi, J.Q., Durucan, S., 2005. A model for changes in coalbed permeability during primary and enhanced methane recovery. SPE Reserv. Eval. Eng. 8 (04), 291–299.
Silin, D., Patzek, T., 2006. Pore space morphology analysis using maximal inscribed spheres. Phys. A Stat. Mech. Appl. 371, 336–360.
Somerton, W.H, Söylemezoğlu, I.M., Dudley, R.C., 1975a. Effect of stress on permeability of coal. Int. J. Rock Mech. Min. Sci. Geomech. Abstr. 12 (5-6), 129–145.
Somerton, W.H., S€oylemezoğlu, I.M., Dudley, R.C., 1975b. Effect of stress on permeability of coal. Int. J. Rock Mech. Min. Sci. 12, 129–145.
Tanikawa, W., Shimamoto, T., 2009. Comparison of Klinkenberg-corrected gas permeability and water permeability in sedimentary rocks. Int. J. Rock Mech. Min. Sci. 46, 229–238.
Vadpour, F., 2009. Nanopores and apparent permeability of gas flow in mudrocks (shales and siltstone). J. Can. Petrol. Technol. 48 (8), 16–21.
Wang, S., Elsworth, D., Liu, J., 2011. Permeability evolution in fractured coal: the roles of fracture geometry and water-content. Int. J. Coal Geol. 87 (1), 13–25.
Wang, Y., Liu, S., Elsworth, D., 2015. Laboratory investigations of gas flow behaviors in tight anthracite and evaluation of different pulse-decay methods on permeability estimation. Int. J. Coal Geol. 149, 118–128.
Wang, L., Wang, S., Zhang, R., Wang, C., Xiong, Y., Zheng, X., et al., 2016a. Review of multi-scale and multi-physical simulation technologies for shale and tight gas reservoirs. J. Nat. Gas Sci. Eng. 37, 560–578.
Wang, L., Wang, S., Zhang, R., Wang, C., Xiong, Y., Zheng, X., et al., 2016b. Review of multi-scale and multi-physical simulation technologies for shale and tight gas reservoirs. J. Nat. Gas Sci. Eng. 37, 560–578.
Wang, L., Wang, S., Zhang, R., Wang, C., Xiong, Y., Zheng, X., et al., 2016c. Review of multi-scale and multi-physical simulation technologies for shale and tight gas reservoirs. J. Nat. Gas Sci. Eng. 37, 560–578.
Wang, K., Du, F., Wang, G., 2017. Investigation of gas pressure and temperature effects on the permeability and steady-state time of chinese anthracite coal: an experimental study. J. Nat. Gas Sci. Eng. 40, 179–188.
Zhang, H., Liu, J., Elsworth, D., 2008. How sorption-induced matrix deformation affects gas flow in coal seams: a new fe model. Int. J. Rock Mech. Mining Sci. 45 (8), 1226–1236.
Zhang, L.J., Li, D.L., Lu, D.T., Zhang, T., 2015. A new formulation of apparent permeability for gas transport in shale. J. Nat. Gas Sci. Eng. 23, 221–226.
Ziarani, A.S., Aguilera, R., 2012. Knudsen's permeability correction for tight porous media. Transp. Porous Media 91, 239–260.